Journal of Atmospheric and Solar-Terrestrial Physics 105-106 (2013) 313–324

Contents lists available at ScienceDirect

Journal of Atmospheric and Solar-Terrestrial Physics

journal homepage: www.elsevier.com/locate/jastp

Ion–neutral coupling in Earth's thermosphere, estimated from concurrent radar and optical observations above Alaska

C. Anderson [a,*], M.J. Kosch [b,c], M.J. Nicolls [d], M. Conde [a]

[a] Geophysical Institute, University of Alaska Fairbanks, Fairbanks, AK 99775, USA
[b] Department of Physics, Lancaster University, United Kingdom
[c] School of Physics, University of KwaZulu-Natal, South Africa
[d] Center for Geospace Studies, SRI International, United States

ARTICLE INFO

Article history:
Received 13 February 2012
Received in revised form
6 April 2013
Accepted 10 April 2013
Available online 25 April 2013

Keywords:
Ionosphere/atmosphere interactions
Auroral ionosphere
Ionospheric dynamics
Thermospheric dynamics

ABSTRACT

During March–April 2011 a campaign of coordinated observations was undertaken between the Poker Flat Advanced Modular Incoherent Scatter Radar and the Poker Flat Scanning Doppler Imager. These instruments provide horizontally resolved maps of plasma and neutral parameters in Earth's thermosphere. We report on data collected during the campaign, and use these data to investigate two key aspects of ion–neutral coupling, namely Joule heating and the ion–neutral collision frequency. Volumetric Joule heating rates were often well correlated with measured ion temperature enhancements. The contribution of the neutral wind dynamo to the observed heating rates was positive when the absolute horizontal magnetic field perturbation ($|\Delta H|$) was less than approximately 40 nT, and negative above that level. The total momentum–transfer ion–neutral collision frequency was estimated to be $1.02^{+0.179}_{-0.152}$ s^{-1} at an altitude of 260 km, which, for a neutral composition of 75% atomic oxygen, yielded an estimate of the O^+–O collision frequency of $0.766^{+0.134}_{-0.114}$ s^{-1}.

1. Introduction

High-latitude plasma motions are strongly influenced by electric fields originating from the magnetosphere. In turn, the neutral thermosphere is coupled to the ionospheric plasma through collisions, which mediate the transfer of momentum and energy between neutral and ionic species. Through ion–neutral coupling, the neutral atmosphere provides a sink for magnetospheric energy via the dissipation of ionospheric currents (e.g. Cole, 1962), and a source of currents through the action of the neutral wind dynamo (e.g. Lyons et al., 1985; Thayer, 1992; Deng et al., 1993).

Investigations of ion–neutral coupling naturally require measurements of both the ion and neutral components. Previous observational studies include those by Nagy et al. (1974), Burnside et al. (1983), Killeen et al. (1984), Rees et al. (1984), Winser et al. (1988), Thayer et al. (1995a), Cierpka et al. (2000), Kosch et al. (2001) and Aruliah et al. (2004, 2005). These studies have frequently relied on point-measurements separated in time and space, from which average flows were calculated, or in some cases fully tristatic (e.g. Aruliah et al., 2004, 2005), but still single-point, measurements. Recently, Kosch et al. (2011) reported on plasma observations made with the EISCAT radar running in a novel dish-scanning mode, which were compared with neutral winds imaged with an all-sky scanning Doppler imager (Griffin et al., 2008). These measurements allowed two-dimensional horizontal ion and neutral flows to be estimated, and mesoscale estimates of Joule heating to be made.

Whereas the EISCAT scanning mode described by Kosch et al. (2011) required 17.8 min to complete a full scan, the Advanced Modular Incoherent Scatter Radar (AMISR) system allows for essentially simultaneous plasma measurements along multiple beams through the use of a phased array. This greatly reduces (and in many cases practically eliminates) the uncertainty in separating out spatial and temporal changes from the measured parameters.

From March 24 through April 5, 2011, a campaign of coordinated observations was conducted between the Poker Flat Advanced Modular Incoherent Scatter Radar (PFISR) and the Poker Flat Scanning Doppler Imager (SDI). These two instruments are located at the Poker Flat Research Range in Alaska (65.12N, 147.43W), and are ideally matched as they both provide simultaneous sampling of upper atmosphere plasma (PFISR) and neutral (SDI) parameters at multiple locations within their respective fields-of-view, with high spatial and temporal resolution. In the current work, data from this campaign were used to investigate two key aspects of high-latitude ion–neutral coupling in the F-region: Joule heating and the ion–neutral collision frequency.

* Correspondence to: Geophysical Institute, University of Alaska Fairbanks, Rm 701B, Fairbanks, AK 99775, USA. Tel.: +1 907 474 5384.
E-mail address: callumenator@gmail.com (C. Anderson).

1364-6826/$ - see front matter © 2013 Elsevier Ltd. All rights reserved.
http://dx.doi.org/10.1016/j.jastp.2013.04.005

2. Instrumentation

2.1. PFISR

The Poker Flat Incoherent Scatter Radar (PFISR) utilizes a phased array to allow pulse-to-pulse electronic beam steering, thereby providing the capability to sample along multiple beam directions essentially simultaneously (Nicolls and Heinselman, 2007). The beam configuration used throughout the campaign is shown in Fig. 1 (red squares show where PFISR beams intersect the 240 km altitude level). This particular beam configuration was chosen to allow two-dimensional (horizontal) ion flow fields to be derived, with the addition of a magnetic field-aligned beam (marked by the blue cross in Fig. 1) for collision frequency calculations (see Section 3.2).

PFISR data during the campaign were collected between 0700 and 1100 UT (~1950–2350 magnetic local time), in the pre-magnetic midnight sector. Eight days were used from the campaign: March 24, 25, 26, 27 and 30, and April 1, 2 and 5. The integration time for one complete sampling (i.e. along all 20 beams) was approximately 3 min. For the Joule heating analysis (Section 3.1) the data were analyzed at this time resolution. For the collision frequency analysis (Section 3.2) the data were post-integrated in time to reduce measurement uncertainties, and the effective integration time of the post-integrated data was approximately 9 min.

The red arrow in the inset panel in Fig. 1 indicates the direction of geomagnetic north. This is the direction normal to the nominal auroral oval at 240 km altitude, as derived from the DGRF/IGRF geomagnetic field model (Gustafsson et al., 1992). With this choice of geomagnetic north, auroral forms are typically aligned with the geomagnetic east–west direction.

2.2. SDI

The Poker Flat Scanning Doppler Imager (SDI) is an all-sky imaging Fabry–Perot spectrometer described by Conde and Smith (1995, 1997). Wide-angle fore-optics combined with a separation-scanned, large-aperture Fabry–Perot etalon and a thermoelectrically cooled, electron-multiplying CCD detector allow the instrument to accumulate spectra from multiple locations or 'zones' across the sky simultaneously. Interference filters are used to isolate wavelengths of interest. A software-controlled filter-wheel enables dynamic filter selection, and in particular allows the spectrometer to observe in a wavelength-interleaved mode, whereby two or more emission wavelengths can be observed in an alternating cycle.

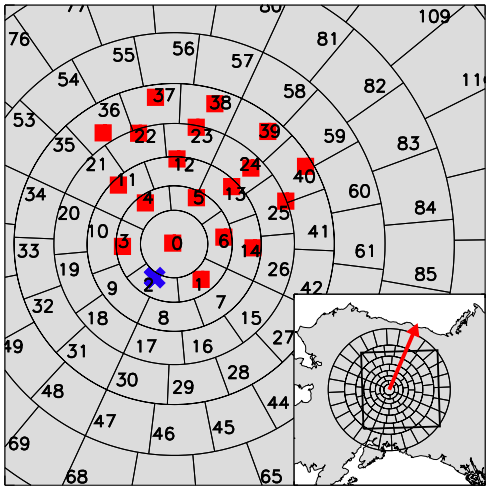

Fig. 1. SDI zones (black numbered annular segments) and PFISR beam positions (red squares and blue cross-marking the magnetic field-aligned beam) on a map of Alaska. Inset shows the full SDI zone map in relation to the Alaskan coastline, with a black rectangle outlining the zoomed-in region shown in the main panel. The red arrow indicates the direction of geomagnetic north (see text). (For interpretation of the references to color in this figure caption, the reader is referred to the web version of this paper.)

The SDI derives geophysical information by least-squares fitting a Gaussian emission profile (convolved with a measured instrument function) to the observed airglow spectra. Fitted parameters are bulk velocity, temperature, emission and continuum intensity. Velocities are derived relative to an assumed zero Doppler reference, which in this study was calculated from the median vertical wind speed over the entire night. This ensures that the final derived vertical winds average to zero over the night, and is a common assumption in the analysis of ground-based neutral wind measurements (see Aruliah and Rees, 1995 for a discussion of this assumption).

For the duration of the campaign the Poker Flat SDI observed in a 557.7/630.0 nm wavelength-interleaved mode, alternating between E-region (557.7 nm) and F-region (630.0 nm) atomic oxygen airglow observations. Only F-region neutral measurements will be presented here. The time resolution of 630.0 nm observations varied during the campaign between approximately 4 and 16 min, as the airglow emission intensity varied. For both the Joule heating and collision frequency analysis, SDI data were linearly interpolated in time where necessary to produce concurrent radar and neutral data.

3. Analysis and results

3.1. Joule heating

In this paper we use the term 'Joule heating' when referring to the dissipation of energy due to ion–neutral relative motion. The volumetric Joule heating rate was calculated three different ways

$$\frac{\partial Q_j^{Eff}}{\partial t} = \sigma_P(\mathbf{E} + \mathbf{u}_n \times \mathbf{B})^2 \tag{1}$$

$$\frac{\partial Q_j^{E}}{\partial t} = \sigma_P \mathbf{E}^2 \tag{2}$$

$$\frac{\partial Q_j}{\partial t} = \mu_{ni}\overline{\nu}_{ni} n_n(\mathbf{u}_n - \mathbf{u}_i)^2 \tag{3}$$

where the superscripts *Eff* ('effective') and *E* serve to distinguish between these three different methods of calculation. Here σ_P is the Pedersen conductivity, n_n the neutral number density, **B** the magnetic field (assumed equal to $B_z = -5 \times 10^5$ nT), **E** the electric field (assumed equal to $-\mathbf{u}_i^F \times \mathbf{B}$, where $\mathbf{u}_i^F$ is the F-region ion drift velocity), $\mathbf{u}_n$ and $\mathbf{u}_i$ the neutral and ion velocity, $\mu_{ni} = m_n m_i/(m_n + m_i)$ is the ion–neutral reduced mass, and $\overline{\nu}_{ni}$ is the mean frequency with which neutral species collide with ions. The Pedersen conductivity was calculated from (Brekke and Rino, 1978)

$$\sigma_P = \frac{n_e q}{|\mathbf{B}|}\frac{\Omega_i \overline{\nu}_{in}}{\Omega_i^2 + \overline{\nu}_{in}^2} \tag{4}$$

where n_e is electron density (assumed equal to the ion density, n_i, by charge neutrality), q the magnitude of the electronic charge, $\overline{\nu}_{in}$ the mean frequency with which ionic species collide with neutrals, and $\Omega_i = q|\mathbf{B}|/m_i$ is the ion gyro-frequency, for an ion of mass m_i. The collision frequency $\overline{\nu}_{in}$ was estimated using (Schunk and Nagy, 2009, pp. 105, 107)

$$\overline{\nu}_{in} = \tfrac{1}{3}[c_0 n(\mathrm{O}) + c_1 n(\mathrm{O_2}) + c_2 n(\mathrm{N_2})] \tag{5}$$

where

$$c_0 = 3.67 \times 10^{-11} T_r^{1/2}(1-0.064 \log_{10}(T_r))^2 \text{ cm}^3 \text{ s}^{-1}$$

$$c_1 = 6.64 \times 10^{-10} \text{ cm}^3 \text{ s}^{-1}$$

$$c_2 = 6.82 \times 10^{-10} \text{ cm}^3 \text{ s}^{-1}$$

and n(O) is the number density of atomic oxygen, etc. The mean neutral-ion temperature is given by $T_r = (T_i + T_n)/2$. Note that the expression for c_0 is the same as that given later in Eq. (21), and was used in the Joule heating calculation as it is a standard empirical formula which provides some height dependence through the T_r term (the collision frequency which will be estimated in Section 3.2 is only valid at a single height). The neutral-ion collision frequency $\bar{\nu}_{ni}$ was then calculated using the relation

$$n_s m_s \nu_{st} = n_t m_t \nu_{ts} \tag{6}$$

for any two species s and t.

Eq. (1) represents the product of the Pedersen conductivity and the electric field in the frame of reference moving with the neutral bulk velocity (the 'effective' electric field), while Eq. (2) assumes that the neutral velocity is negligibly small, a common assumption when collocated neutral wind measurements are unavailable. Eq. (3) estimates the rate of heating directly from the ion neutral relative motion. Note that the squared term in Eq. (1) differs from that in Eq. (3) only in the height at which the ion velocity is estimated. In the current study, this height difference had a negligible impact on the ion velocity, therefore Eqs. (1) and (3) can be considered approximately equivalent in this study.

Ion drift velocities were derived using the method described by Semeter et al. (2010). The PFISR field-of-view (see Fig. 1) was divided into a horizontal 4×4 grid of overlapping cells. The overlap was set at 50% of the cell size, thereby imposing a spatial smoothness constraint on the derived flow velocities. Radar line-of-sight velocity samples between 200 and 400 km altitude were projected onto this grid and the 2-dimensional flow vector within each cell estimated using Bayesian inversion (see Semeter et al., 2010, for details). For each grid cell, a neutral wind estimate was obtained from the SDI viewing zone which was closest (geographically) to the center of that cell. Neutral wind vectors were derived from the spatial variation of the measured line-of-sight wind, as described by Conde and Smith (1998).

Having estimated the Joule heating rate the ion temperature can be modeled by (e.g. Banks and Kockarts, 1973, p. 243)

$$T_i \simeq T_n + \frac{\langle m_n \rangle}{3k}(\mathbf{u}_n - \mathbf{u}_i)^2 \tag{7}$$

That is, the mean ion temperature (averaged over the grid) is approximately equal to the neutral temperature (also averaged over the grid) plus the contribution from frictional heating (k is the Boltzmann constant). Eq. (7) assumes steady-state, incompressible ion motion, and neglects heat advection, heat conduction, relative ion–electron motion and heat exchange with the electron gas. These assumptions are considered valid at altitudes below approximately 400 km, and for length and time scales greater than ≈15 km and a few seconds respectively (e.g. St.-Maurice et al., 1999). Since the ion temperature is measured by the radar, direct comparison with Eq. (7) is possible (cf. Cierpka et al., 2000).

Fig. 2 shows examples of derived ion drift (red arrows) and neutral wind (black arrows) during a 1-h period on April 5, 2011. This example is interesting because the ion–neutral flow was tightly coupled between 0929 and 1007 UT, during which time both neutral winds and ion drifts rotated from approximately magnetic westward to magnetic southwestward flow. In the panels at 0955 and 1007 UT small-scale curvature is evident in both the ion and neutral flow. From 1020 UT until the end of observations (at 1100 UT) the ion flow reverted to predominantly magnetic westward flow while the neutral winds continued to rotate toward magnetic southward flow. In the magnetic midnight sector the neutral F-region flow above Alaska is usually dominated by the emergence on the nightside of the antisunward cross-polar

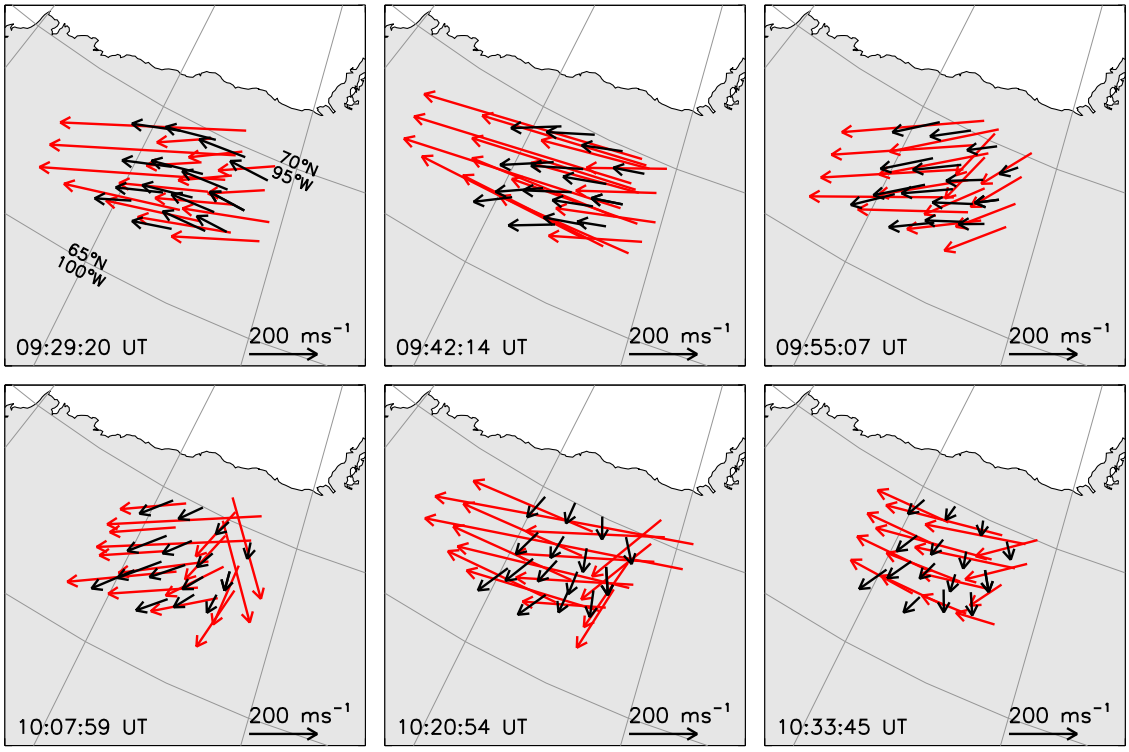

Fig. 2. Ion drift vectors (red) and neutral winds (black) from April 5, 2011, overlaid onto a map of Alaska (grey shaded region). Light grey lines show magnetic latitude and longitude (coordinates are given in the first panel, top left). (For interpretation of the references to color in this figure caption, the reader is referred to the web version of this paper.)

cap flow, and this feature was becoming increasingly dominant in the neutral wind fields shown in Fig. 2 as time progressed.

The altitude to which neutral wind and temperature measurements made by the SDI correspond depends upon the height profile of the airglow emission intensity. In order to extract radar measurements at the same altitude as the neutrals, it is necessary to estimate the altitude of peak airglow emission. The 630.0 nm airglow height-profile was modeled using the equation of Sobral et al. (1993), with model coefficients as found in de Meneses et al. (2008). The mean peak airglow altitude throughout the campaign (excluding April 1 and 2, see below) was 260 km, with a standard deviation of 6.5 km.

On two days during the campaign (April 1 and 2), the electron density profiles that were used as input to the airglow model did not follow the clear Chapman-like profile that was observed during the rest of the campaign, and at these times the modeled airglow peak emission altitude was reduced to 220 km. This resulted in the measured ion temperature (interpolated to the modeled peak height) being systematically 100–200 K lower than the neutral temperature at those times, indicating that the modeled altitude was likely incorrect.

E-region neutral temperatures measured by the SDI (at 557.7 nm) on April 1 and 2 were approximately 100–200 K above typical E-region (120 km altitude) temperatures. On April 1, for example, a temperature enhancement of 200 K occurred over approximately 3 h. Considerable experience stretching back over a decade of 557.7 nm Doppler temperature observations (see for example Holmes et al., 2005) indicates that this temperature increase was due to variation in the E-region peak airglow emission altitude, caused by a significant contribution from soft electron precipitation. The strong temperature gradient in the E-region makes temperatures inferred from 557.7 nm airglow measurements very sensitive to changes in the peak emission height. In addition, such a large temperature increase, if it were due to actual in-situ heating (for example Joule heating), would necessarily be associated with sustained upward vertical motion, as the local hydrostatic balance would have been significantly perturbed. No sustained vertical winds of significant magnitude were observed during the periods of temperature increase, thus we attribute these temperature enhancements to airglow peak height variation caused by soft electron precipitation.

Assuming a dominant contribution from soft electron precipitation in the F-region at these times, the peak 630.0 nm airglow emission altitude would likely lie above 240 km, typically between 250 and 300 km (see for example Figure 4 of Roble and Rees, 1977). Since the airglow model was unable to provide reliable estimates of airglow peak height on April 1 and 2, we manually selected a peak altitude which resulted in the best agreement between modeled ion temperature (Eq. (7)) and measured ion temperature. The peak emission altitude which resulted in the best agreement on those nights was 270 km.

Having obtained time-series of peak airglow emission altitude, radar data were linearly interpolated to that altitude or, in the case of the electron density, were calculated directly from a fitted Chapman function (see Section 3.2). In evaluating Eqs. (1) and (3), the ion–neutral velocity difference (squared) was taken as the median of $(\mathbf{u}_n-\mathbf{u}_i)^2$ calculated from the winds derived in each grid cell. Neutral number densities at the peak airglow altitude were obtained from the empirical NRLMSISE-00 atmospheric model.

Figs. 3 and 4 summarize the Joule heating analysis over 8 days of the campaign. Note that the days are not all consecutive, as cloud or poor data quality precluded the inclusion of 5 other days. Panels in these figures are labelled A–F, and show: (A) the median vector velocity difference in geomagnetic coordinates (averaged over all grid cells), (B) the neutral temperature (black), measured ion temperature (blue), predicted ion temperature from Eq. (7) (red) and the NRLMSISE-00 modeled (green) temperature, (C) the volumetric Joule heating rate calculated using Eqs. (1) (red), (2) (blue) and (3) (black), (D) the electron density (black) and 630.0 nm airglow emission intensity (red), (E) the modeled peak airglow altitude (black) and calculated σ_P (red), and (F) the Dst index (red) and absolute magnetic field perturbation (black).

The first four days of the campaign (Fig. 3) were magnetically quiet, however appreciable heating was observed on March 24 and 25, of approximately the same peak magnitude and during the same UT time period. Both of these periods corresponded to times of increased shear in the neutral wind field associated with minor auroral activity (note that the change in neutral wind speed over the PFISR field-of-view caused by this shear was not significant). All three estimates of the Joule heating rate agreed closely during the period of peak heating, and the predicted ion temperatures (red) showed good agreement with the measured ion temperatures.

On March 26 and 27, when local magnetic activity was extremely low and heating rates correspondingly small, the predicted ion temperature showed negligible enhancement over the neutral temperature, which did not agree well with the time-variations of the measured ion temperature, despite the absolute values of both ion and neutral temperatures being close (median difference was 44 K on March 26 and 77 K on March 27). We note that the ion temperatures may be affected by the assumptions underlying the ion composition model, which may influence the comparison.

The last three days in Fig. 4 showed elevated levels of magnetic activity, particularly April 2. Heating rates on April 2 were elevated between 0700-0830 and 0930-1030 UT, associated with significant meridional shear in the neutral zonal flow. Modeled ion temperatures showed good agreement with the measured ion temperature. Average neutral temperatures on April 1 and 2 were also elevated, likely due to the increased levels of geomagnetic activity associated with the minor storm period of April 2–5, as indicated by the Dst index.

Variations in modeled emission altitude can affect the Joule heating rate (derived from Eqs. (1)–(3) through changes in the Pedersen conductivity and neutral density. However the magnitude of the altitude variations observed during the campaign were small (generally less than 20 km), and from this we conclude that the variations in the Joule heating rates shown in Figs. 3 and 4 are dominated by actual in-situ heating, and are not simply due to changes in airglow emission altitude (although this effect will be present to a small degree whenever the emission peak is time-varying).

3.2. Collision frequency

The ambipolar diffusion velocity for a major ion species is given by (see for example Schunk and Nagy, 2009)

$$u_i^{\parallel} = u_n^{\parallel} - D_a\left[\frac{1}{n_i}\frac{\partial n_i}{\partial r} + \frac{1}{T_p}\frac{\partial T_p}{\partial r} + \frac{m_i g^{\parallel}}{2kT_p}\right] \tag{8}$$

where the $\parallel$ superscript refers to the magnetic field-aligned direction, r is a coordinate along this direction (with the positive direction in the sense of increasing altitude), i and n refer to ion and neutral species, and $T_p = (T_i + T_e)/2$ is the plasma (mean ion/electron) temperature. The ambipolar diffusion coefficient D_a is given by

$$D_a = \frac{2kT_p}{m_i \nu_{in}} \tag{9}$$

Following Wickwar et al. (1984, Appendix), the effect of ion composition is included by replacing m_i with $\langle m_i \rangle$ and $m_i\nu_{in}$ with $\langle m_i\nu_{in}\rangle \approx \langle m_i\rangle\langle\nu_{in}\rangle$. Eqs. (8) and (9) can then be combined to give the

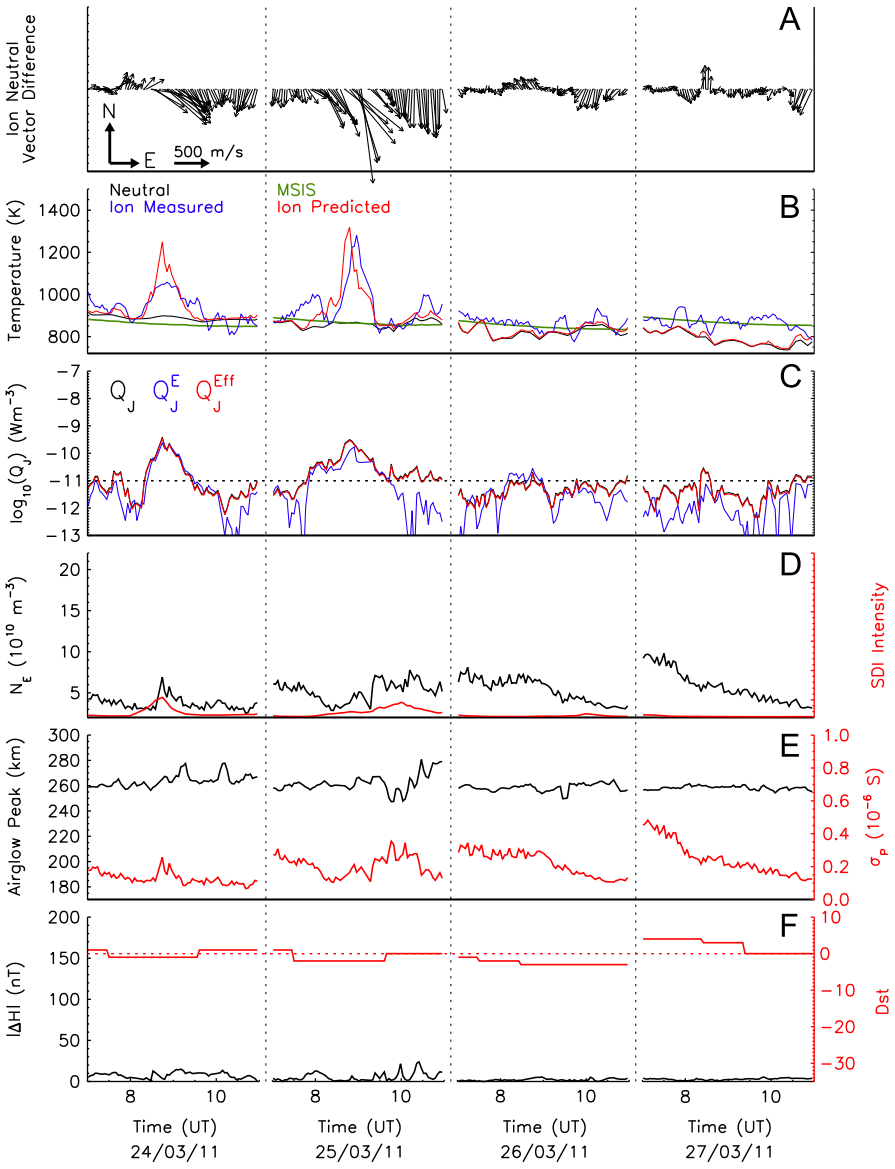

Fig. 3. Summary of Joule heating calculation during the campaign. Panels show: (A) ion–neutral vector difference, (B) temperature (neutral—black, ion measured—blue, ion predicted—red, NRLMSISE-00 modeled—green), (C) Joule heating rate calculated using Eqs. (1) (red), (2) (blue) and (3) (black), (D) electron density (black) and airglow emission intensity (red), (E) modeled airglow peak emission altitude (black) and Pedersen conductance (red), and (F) the Dst index (red) and absolute magnetic field perturbation $|\Delta H|$ (black). Each column of the figure shows a different day, indicated at the bottom of the plot. (For interpretation of the references to color in this figure caption, the reader is referred to the web version of this paper.)

total momentum–transfer ion–neutral collision frequency

$$\langle \nu_{in} \rangle = \frac{2kT_p}{\langle m_i \rangle (u_n^{\parallel} - u_i^{\parallel})} \left[\frac{1}{n_i} \frac{\partial n_i}{\partial r} + \frac{1}{T_p} \frac{\partial T_p}{\partial r} + \frac{\langle m_i \rangle g \sin(I)}{2kT_p} \right] \tag{10}$$

where $I \approx 77.5^\circ$ is the inclination of the geomagnetic field. All quantities on the right-hand side of Eq. (10) were measured in the present study, except for the ion mass. The ion mass was estimated using the composition weighted mass average, where the ion composition was calculated using a photochemical model (Richards et al., 2009, 2010) and the measured n_e. At the altitudes of interest in this study, median $\langle m_i \rangle$ throughout the campaign was within 20% of the oxygen mass, thus for simplicity in what follows, we assume that $\langle \nu_{in} \rangle \approx \nu_{O^+n}$, and we denote this quantity by ν_{in}.

The location at which the magnetic field-aligned direction crosses 240 km altitude is shown by the blue cross in Fig. 1. Radar measurements from this field-aligned beam and neutral measurements from the SDI zone 2 were used in the collision frequency analysis. Radar data were linearly interpolated where necessary to the modeled airglow peak altitude (as described in Section 3.1). The electron/ion density gradient $\partial n_i / \partial r$ was calculated by first fitting a Chapman function to the measured $n_e(r) = n_i(r)$ profile, following the method described by Burnside et al. (1983). This function has the form

$$N(r) = a_0 \exp(a_1[1 - f - a_2 \exp(-f)]) \tag{11}$$

where

$$f = \frac{z - z_0}{H} \tag{12}$$

$$H = H_0 + \beta(z - z_0) \tag{13}$$

In these equations z is the altitude, which is related to the range r by $z = r \cos(\theta)$, with θ the zenith angle of the radar beam under consideration. The peak of the height profile is determined by z_0, while H_0 represents a scale-height, and the remaining coefficients a_0, a_1, a_2, β control the magnitude and shape of the height profile.

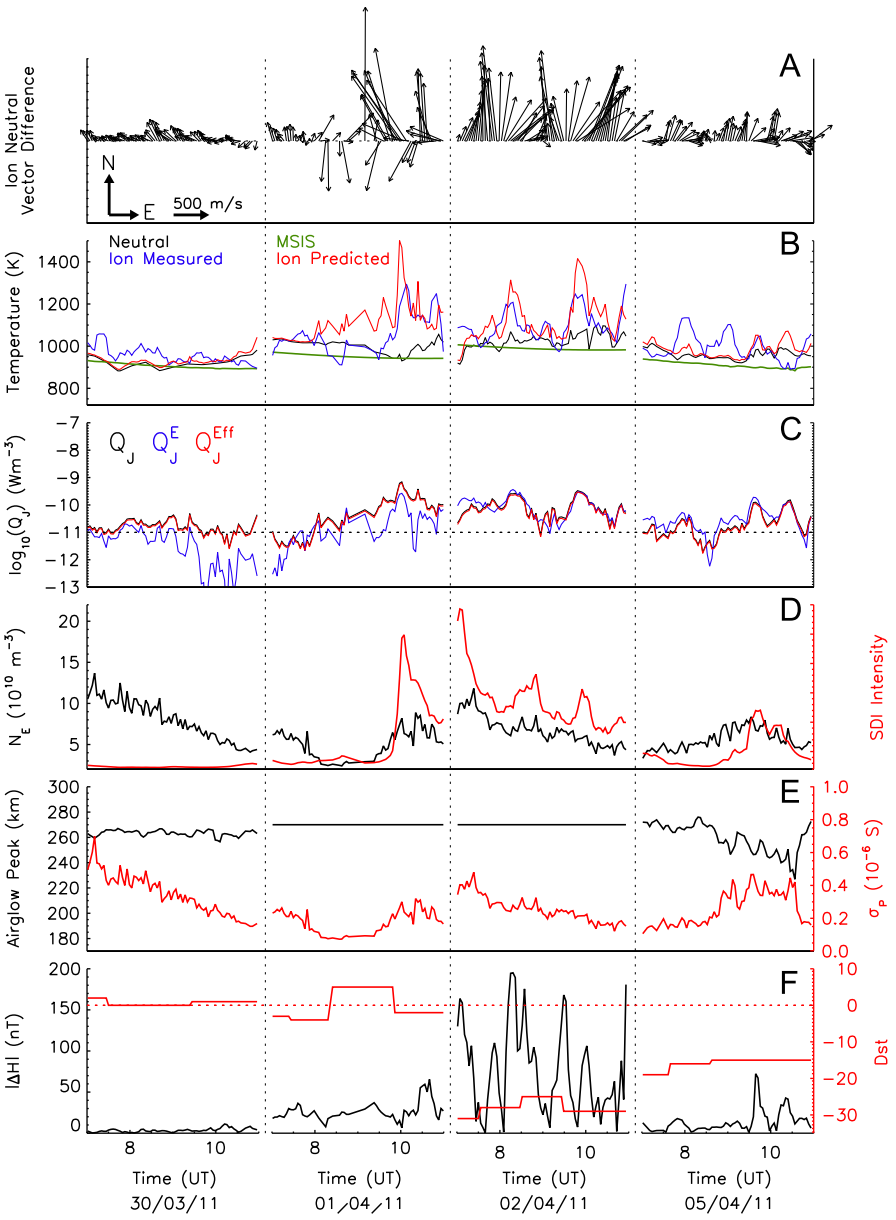

Fig. 4. Same format as Fig. 3.

A weighted non-linear least-squares fit of Eq. (11) to the measured $n_i(r)$ (weighted by the inverse of the measurement uncertainties) gave a set of best-estimates for the 6 coefficients $\{a_0, a_1, a_2, z_0, H_0, \beta\}$. The analytic derivative of Eq. (11) was then used to estimate $\partial n_i/\partial r$. On April 1 and 2 the Chapman profile did not fit the measured n_e well, and on these days linear interpolation was used to calculate n_i at the airglow altitude, and finite-differencing used to estimate $\partial n_i/\partial r$. Again following Burnside et al. (1983), the gradient of T_p was estimated with a linear fit to the measured $T_p(r) = (T_e(r) + T_i(r))/2$. Representative examples of fitted $N(r)$ and $T_p(r)$ profiles are shown in Fig. 5.

The derivation of Eq. (10) assumes that the momentum balance is in a steady-state by neglecting the time-derivative of the ion and electron velocity (and thereby neglecting waves). Advection is also neglected, as is the divergence of the ion stress tensor along the field aligned direction, heat flow, centripetal and Coriolis acceleration, and externally imposed parallel electric fields. It is therefore only valid under very quiet geomagnetic conditions, for which the assumptions listed above are most likely to be satisfied. Such conditions are very difficult to attain at auroral latitudes, where ionospheric currents and plasma convection can be highly variable in space and time (e.g. Heppner et al., 1993).

In order to estimate the value of each of the parameters on the right-hand-side of Eq. (10) under very quiet geomagnetic conditions, the following procedure was used. First, local geomagnetic activity was quantified by the magnitude of the horizontal magnetic field deviation measured by the Poker Flat magnetometer ($|\Delta H|$). Then, each of the parameters were sorted into $|\Delta H|$ bins of width 8 nT, and medians taken over each bin. For $|\Delta H| < 40$ nT (see Fig. 6 for the distribution of magnetic activity during the campaign) the trends followed by the medians were approximately linear, therefore least-squares linear regression was used to fit a simple linear model ($y = a|\Delta H| + b$), and the 'low activity' estimate of the given parameter (y) was then given by b (since $y = b$ for $|\Delta H| = 0$). The uncertainty in y was estimated by the 1σ uncertainty in the fitted coefficient b. The binned parameters and fitted linear models are shown in Fig. 7.

Table 1 lists the fitted 'zero activity' estimates of each parameter, and the associated 1σ uncertainty. These estimates were then used to solve Eq. (10) directly. Monte-Carlo simulation was

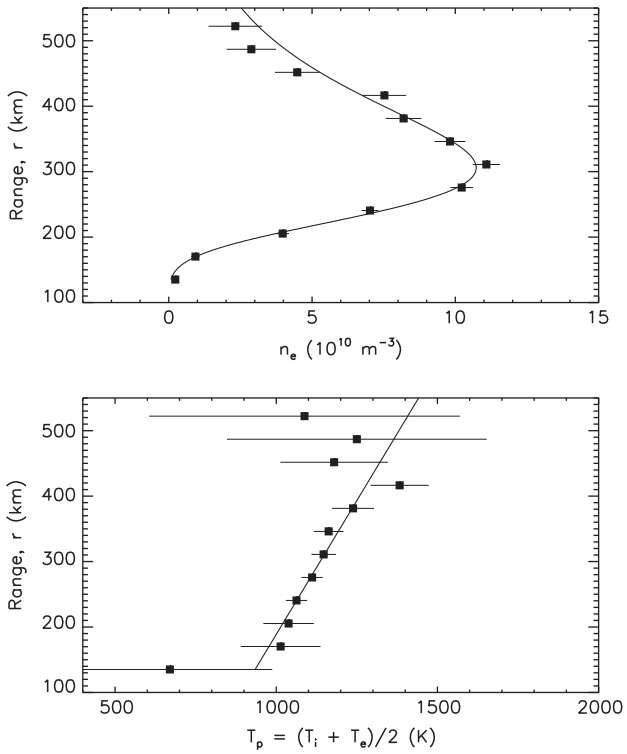

Fig. 5. Top panel: measured electron density n_e (black squares) and associated uncertainties (error-bars), with the fitted profile of Eq. (11) overlaid. Lower panel: measured T_p and associated uncertainties (error-bars) with linear fit overlaid. Note that measurements with large uncertainties are given low weight during the fitting process, and at the latitudes of interest (200–300 km), uncertainties are generally low.

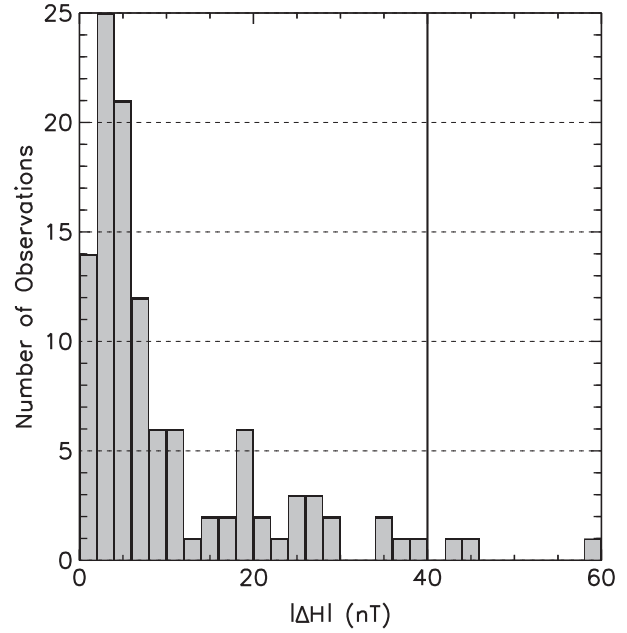

Fig. 6. Histogram of magnetic activity as parameterized by $|\Delta H|$. Only observations corresponding to values of $|\Delta H| < 40$ (indicated by the solid vertical line) were used in the collision frequency calculation. Note that higher levels of $|\Delta H|$ were recorded during the campaign, however the number of such measurements was very low, and thus the distribution shown here is terminated at 60 nT. Note also that this figure corresponds to the post-integrated (lower time-resolution) PFISR data (see Section 2.1).

used to estimate the uncertainty in the derived ν_{in}. Random, normally distributed populations of each of the parameters in Table 1 were generated, where each population had a mean equal to the value in column 2 of the table and standard deviation equal to the uncertainty shown in column 3. Values of ν_{in} were then calculated from 1 000 000 random samples from each population. The resulting distribution of ν_{in} was approximately log-normal, for which the estimate of uncertainty was the standard deviation of the natural logarithm of the variable

$$\mu_\nu = \frac{1}{N}\sum_{0}^{N-1} \ln(\nu_{in}) \tag{14}$$

$$\sigma_\nu = \sqrt{\frac{1}{N}\sum_{0}^{N-1} [\ln(\nu_{in}) - \mu_\nu]^2} \tag{15}$$

where $N = 1\,000\,000$. Estimates of the upper and lower 1σ bounds of the calculated ν_{in} were then given by

$$\pm \delta\nu_{in} = \nu_{in} e^{\pm \sigma_\nu} \tag{16}$$

The final collision frequency estimate was

$$\nu_{in} = 1.02^{+0.179}_{-0.152}\ \mathrm{s}^{-1} \tag{17}$$

where the asymmetry of the uncertainties arises from the non-Gaussian distribution of ν_{in}.

The modeled emission altitude and atomic oxygen fractional number density (estimated from NRLMSISE-00) were extrapolated back to the assumed 'zero activity' level in the same manner as the parameters in Table 1. The altitude to which the collision frequency given by Eq. (17) corresponds is 260 km. This estimate for ν_{in} represents the total momentum–transfer collision frequency for a major ion (in this case O^+) at an altitude of 260 km (the estimated 'zero activity' altitude), and therefore contains contributions from all neutral species. However, the composition at F-region altitudes is dominated by atomic oxygen, and therefore the ion–neutral collision frequency is dominated by the resonant charge exchange reaction between O^+ and O. There has been some argument as to the correct empirical expression for the O^+–O collision frequency (see the discussion in Section 4.2).

The fractional composition of atomic oxygen at 260 km (at the assumed 'zero activity' level) was approximately 75%. With this estimate of the composition, we estimate the O^+–O collision frequency as

$$\nu_{(O^+,O)} = 0.766^{+0.134}_{-0.114}\ \mathrm{s}^{-1} \tag{18}$$

4. Discussion

4.1. Joule heating

One important result of the Joule heating analysis is the magnitude of the contribution of the neutral dynamo to the electric field. Neglecting the neutral wind often led to an underestimation of the Joule heating rate. Fig. 8 shows the fractional difference between the Joule heating rates calculated using Eqs. (1) and (2)

$$\Delta Q = \frac{Q_J^{Eff} - Q_J^{E}}{Q_J^{Eff}} \tag{19}$$

ΔQ was averaged over the eight days of the campaign, as a function of magnetic local time, using time bins of width 20 min. On average the neutral wind dynamo accounted for 36% of the effective Joule heating rate (Q_J^{Eff}), which compares well with the contribution of 29% derived by Aruliah et al. (2005). Taking the absolute value of ΔQ (thereby considering only the magnitude of the neutral wind dynamo contribution to the electric field, regardless of the sign of that contribution), the median of $|\Delta Q|$ was 64%. This indicates that the neutral wind can effect a

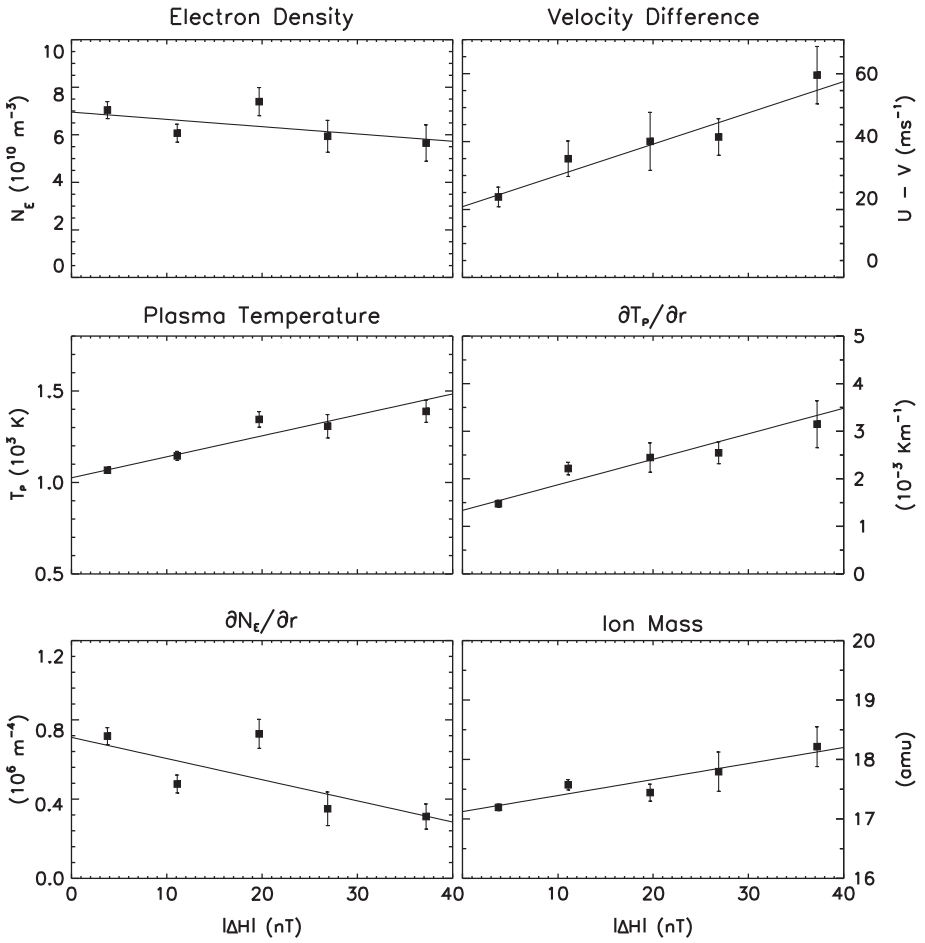

Fig. 7. Observations binned by magnetic activity ($|\Delta H|$). Data points show the median of each parameter within the given magnetic activity bin, with error-bars indicating the standard error of the distribution within each bin. Solid lines show linear trends fitted to the binned data.

Table 1
'Zero activity' parameter estimates.

Parameter	Value ($\|\Delta H\| = 0$)	1σ Uncertainty
n_i	6.95×10^{10} m^{-3}	3.53×10^{9} m^{-3}
$\partial n_i/\partial r$	7.11×10^{5} m^{-4}	4.05×10^{4} m^{-4}
T_p	1030 K	13.6 K
$\partial T_p/\partial r$	1.33×10^{-3} K m^{-1}	8.79×10^{-5} K m^{-1}
$u_n^{\parallel} - u_i^{\parallel}$	20.8 m s^{-1}	3.18 m s^{-1}
m_i	17.1 amu	0.0670 amu

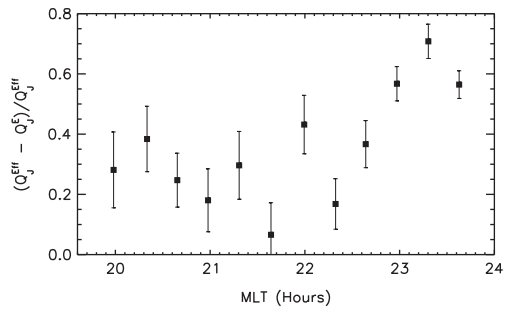

Fig. 8. The contribution of the neutral wind dynamo to the effective Joule heating rate, averaged over the eight days shown in Figs. 3 and 4. Note that these are averages of the signed quantity ΔQ as defined in Eq. (19). Data were averaged over 20 min time bins. Error-bars show the standard error of the mean within each bin.

significant modification of the electric field, as suggested, for example, by Thayer (1992). Fig. 8 also shows a systematic variation with local (magnetic) time, with the neutral wind contribution peaking around an hour before magnetic midnight. The data presented by Aruliah et al. (2005) for a single night also showed a peak in the neutral wind contribution, however in that case the peak occurred closer to 0300 MLT.

The averages in Fig. 8 are dominated by quiet magnetic conditions, for which the neutral wind contribution was generally positive (i.e. the effect of the dynamo was to increase the electric field). However, under elevated levels of magnetic activity, the effect of the neutral dynamo was often to reduce the effective Joule heating rate, as can be seen from Fig. 9. The same trend was observed by Cierpka et al. (2000), from data recorded on two nights in November 1998. In that study distributions of $Q_J^E - Q_J^{Eff}$ were strongly peaked at positive values (indicating a *negative* contribution from the neutral dynamo) under active conditions ($K_P = 7-, 5-$), and negative values under quiet conditions ($K_P = 0+, 0$), however the quiet-time distribution was less strongly peaked than the active-time distribution.

Thayer et al. (1995b) simulated the effect of the neutral dynamo on the electromagnetic energy flux under moderate to quiet geomagnetic activity (11 GW hemispheric power, solar $F_{10.7} = 220 \times 10^{-22}$ W m^{-2} Hz^{-1}). These authors observed that the effect of the neutral wind was to reduce the Joule heating rate (by as much as a factor of 3), particularly over the polar cap. In the current dataset, hemispheric power (obtained from NOAA POES satellite measurements) was ≥11 GW for $|\Delta H| \geq 30$ nT, which is

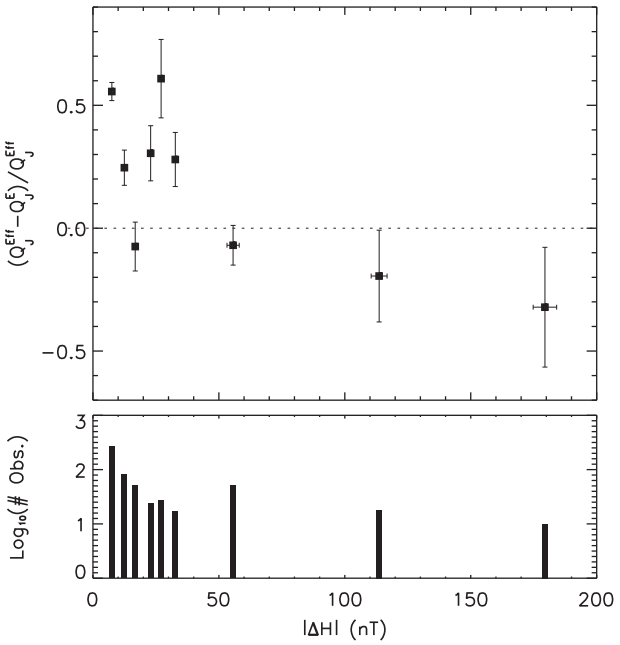

Fig. 9. Top panel: the contribution of the neutral wind dynamo to the effective Joule heating rate as a function of magnetic activity. The $|\Delta H|$ bin width for averaging was 5 nT for low activity ($|\Delta H| < 30$) and 60 nT for higher activity levels ($|\Delta H| \geq 30$). Error-bars show the standard error of the mean. Bottom panel: the number ($\log_{10}$) of observations within each magnetic activity bin.

close to the transition region between positive and negative neutral wind contribution in Fig. 9. Taking into account the greater level of solar activity in the simulation ($F_{10.7}$ during the campaign was approximately 110×10^{-22} W m^{-2} Hz^{-1}), the simulations reported by Thayer et al. (1995b) show some qualitative agreement with the results presented in the current work. A larger dataset covering a wider range of geomagnetic conditions would be required to investigate these relationships in more detail.

We also note that during periods of enhanced Joule heating, the ion temperature predicted by Eq. (7) often agreed well with the ion temperature measured by the radar. Cierpka et al. (2000) observed similarly good agreement between modeled and measured ion temperatures. In the current work, however, at times when the Joule heating rate was low, the measured ion temperature was frequently higher than that predicted from Eq. (7), since at those times the predicted temperature was essentially the neutral temperature. This may have been caused by a failure of the airglow model used in this work to accurately capture variations in the peak airglow emission altitude, which would mean that the measured temperatures displayed in Figs. 3 and 4 at those times did not correspond to the altitude at which neutral measurements were made. For example, on March 26 and 27, there were periods where the ion temperature was approximately 100 K above the neutral (and predicted ion) temperature, whereas it was well modeled by NRLMSISE-00 at the predicted airglow altitude. It is possible that at those times the airglow emission was coming from a lower altitude than predicted, giving rise to a systematic offset, or that other (significant) sources of ion heating were present which were not accounted for in the model.

4.2. Collision frequency

The efficiency of the ion–neutral coupling process is quantified by the collision frequency, ν_{in}. This parameter controls the formation of the F2-layer via plasma diffusion (Moffett et al., 1990), and the strength of the ion–neutral momentum–transfer and heating terms in the atmospheric equations of motion and energy. It is thus a critically important quantity for first-principles based upper-atmospheric models.

A number of authors have investigated the ion–neutral collision frequency at E-region altitudes (e.g. Schlegel et al., 1980; Lathuillére et al., 1983; Fla et al., 1985; Huuskonen et al., 1986; Kirkwood, 1986; Nygrén, 1996; Sangalli et al., 2009; Burchill et al., 2012), and found them to be in reasonable agreement with values derived empirically using modeled atmospheric densities. At F-region altitudes, however, agreement with empirically modeled values has been variable.

The collision frequency at F-region altitudes is dominated by the resonant charge exchange reaction between O^+ and O. Various expressions for the frequency of this collision have been derived from theoretical principles. The calculations of Stubbe (1968), Stallcop et al. (1991) and Pesnell et al. (1993) have resulted in expressions for the collision frequency that agree to within a few percent (Omidvar et al., 1998). Hickman et al. (1997) improved upon these theoretical expressions by including fine structure effects, and the empirical fit to their results was given by

$$\nu_{(O^+,O)} = 5.92 \times 10^{-11}\ n(O) T_r^{0.393} \left[1 + \left(\frac{96.6}{T_r}\right)^2\right] \quad (20)$$

where n(O) is the number density of atomic oxygen (in cm^{-3}). An earlier expression for the collision frequency, which has often been cited in the literature, was given by Schunk and Walker (1973)

$$\nu_{(O^+,O)} = 3.67 \times 10^{-11}\ n(O) T_r^{1/2} (1 - 0.064 \log_{10} T_r)^2 \quad (21)$$

Empirical estimates of $\nu_{(O^+,O)}$ from observational data have however shown some discrepancy with the theoretical expressions (see Salah, 1993 for a concise review). A statistical method due to Burnside et al. (1987) has been most commonly used to estimate $\nu_{(O^+,O)}$ from concurrent plasma and neutral measurements. This method attempts to minimize the residual between a modeled neutral meridional wind (employing radar data and the ambipolar diffusion equation) and the directly measured neutral wind (usually from Fabry–Perot interferometer measurements). The parameter which is varied is a scaling factor for $\nu_{(O^+,O)}$.

From measurements made at Arecibo (lat. 18°), Burnside et al. (1987) concluded that the collision frequency given by Eq. (21) should be scaled by a factor $F = 1.7^{+0.7}_{-0.3}$. A number of other observational studies have also indicated that an increase in the ion–neutral collision frequency as parameterized by Eq. (21) (or similar parameterizations by other authors, see Salah, 1993 and references therein) was required. These studies were carried out at Arecibo and Millstone Hill, i.e. at low to mid latitudes.

At auroral latitudes, Winser et al. (1988) estimated collision frequencies directly from the ambipolar diffusion equation (Eq. (8)), using incoherent scatter radar (EISCAT) measurements of the plasma and Fabry–Perot measurements of the neutral wind. These authors derived ion–neutral collision frequencies which were approximately a factor of 3 *lower* than those modeled by Eq. (21). A later study by Davis et al. (1995), using the technique described by Burnside et al. (1987), derived a scaling factor of $F = 1.2$. These authors also pointed out that measurement noise tends to increase the derived value of F, a conclusion also reached by Reddy et al. (1994). Recently, Wu et al. (2012) have used a balloon-borne Fabry–Perot spectrometer in conjunction with EISCAT measurements to estimate a daytime Burnside factor of $F = 0.85^{+0.55}_{-0.30}$.

The weight of observational evidence supporting an increase in the parameterized $\nu_{(O^+,O)}$ resulted in the recommendation of an interim standard collision frequency, primarily to facilitate intercomparison between different incoherent scatter radar wind measurements. The expression for the interim standard was given

by (Salah, 1993)

$$\nu_{(O^+,O)} = 4 \times 10^{-11}\ T_r^{1/2} n(\mathrm{O}) \quad (22)$$

This expression was derived by scaling an earlier expression due to Dalgarno (1964), which is approximately equal to that given by Eq. (21) over the temperature range of interest.

Since the ion–neutral collision frequency depends most critically on the neutral density, which is not expected to vary considerably over the time scales of interest here, the statistical technique of Burnside et al. (1987) has the advantage of using multiple data points to produce a robust estimate of the scaling parameter F, and hence $\nu_{(O^+,O)}$. However, it is not always clear how well the modeled neutral winds match those which are directly observed, even after the residual has been minimized. In contrast, the direct calculation of Winser et al. (1988) provides time-dependent estimates of $\nu_{(O^+,O)}$, however it is exceedingly sensitive to (in particular) uncertainties in the ion–neutral velocity difference term of Eq. (10).

The method used in the present work provides an alternative way of estimating the collision frequency, whereby statistical regression is used to estimate values for the parameters in Eq. (10) under the lowest levels of geomagnetic activity, and these are then used in the 'direct' calculation of $\nu_{(O^+,O)}$. Time-dependence is sacrificed for improved statistical confidence in the terms of the ambipolar diffusion equation, and estimates are obtained for each of those terms under conditions for which the diffusion equation is most likely to be valid.

To place the current estimate of $\nu_{(O^+,O)}$ (Eq. (18)) in the context of the empirical expressions given above, the 'zero activity' estimates of the $\nu_{(O^+,O)}$ from each of the expressions given by Eqs. (20)–(22) have been calculated in the same manner as the parameters in Fig. 7. The comparison of these results is given in Table 2 (note that all results refer to the zero-activity altitude of 260 km). The uncertainties for the model values given in the table are the 1σ uncertainties in the linear regression, and do not reflect the much larger systematic uncertainty in the estimates of neutral density, which have been derived from NRLMSISE-00.

The result derived in the current paper falls between the estimates given by Hickman et al. (1997) and Schunk and Walker (1973) expressions, which are both within the limits of our experimental uncertainty (in fact both estimates are 0.54σ away from our value). The value given by Salah (1993) expression is approximately 2.9σ greater than our estimate. With a larger dataset, the statistical uncertainties in our estimate of $\nu_{(O^+,O)}$ should decrease, and possibly allow us to discriminate between Hickman et al. (1997) and Schunk and Walker (1973) expressions.

The experimental value of $\nu_{(O^+,O)} = 0.766^{+0.134}_{-0.114}$ can be used to estimate the atomic oxygen number density (corresponding to an altitude of 260 km), by rearranging one of the empirical expressions for $\nu_{(O^+,O)}$. For example, by rearranging Eq. (20), we obtain

$$n(\mathrm{O}) = 9.26^{+1.62}_{-1.38} \quad (10^8\ \mathrm{cm}^{-3}) \quad (23)$$

Extrapolating the NRLMSISE-00 estimates of n(O) back to the 'zero activity' level gives:

$$n(\mathrm{O})_{\mathrm{msis}} = 9.75^{+0.115}_{-0.115} \quad (10^8\ \mathrm{cm}^{-3}) \quad (24)$$

The model and experimental estimates of atomic oxygen number density are therefore close, and provide an additional check on the self-consistency of the calculations. Finally, these estimates for the oxygen number density can be used to arrive at an estimate of the Burnside factor, for which we obtain

$$F = 0.950^{+0.179}_{-0.151} \quad (25)$$

We note that this value is close to that estimated by Wu et al. (2012), taking into account the experimental uncertainties in both values.

Table 2
$\nu_{(O^+,O)}$ comparison.

$\nu_{(O^+,O)}$ (s^{-1})	$\pm 1\sigma$ (s^{-1})	Source
1.16	0.027	Salah (Eq. (22))
0.838	0.017	Hickman (Eq. (20))
0.766	+0.134, −0.114	Current work
0.704	0.015	Schunk (Eq. (21))

5. Conclusion

A coordinated campaign of observations between the Poker Flat Advanced Modular Incoherent Scatter Radar (PFISR) and the Poker Flat Scanning Doppler Imager (SDI) was conducted between March 24 and April 5, 2011. These instruments have the capability to map two-dimensional (horizontal) temperature and flow structures in the plasma (PFISR) and neutral (SDI) components of the upper atmosphere. Data from this campaign were used to investigate ion–neutral coupling in the high-latitude (auroral) F-region, specifically Joule heating and the ion–neutral collision frequency.

The key findings from this study are summarized below

1. Volumetric Joule heating rates often correlated well with enhancements in the ion temperature. Predicted ion temperatures often showed good agreement with measured ion temperatures during periods of enhanced Joule heating, however, when heating rates were low, measured ion temperatures were generally higher than those predicted, possibly due to uncertainties in the modeled peak airglow altitude.
2. The average neutral wind dynamo over the entire data set contributed on average 36% of the effective Joule heating rate. In absolute terms, the contribution of the neutral dynamo (neglecting the difference between positive and negative contributions) was 64%, highlighting the important role that neutral dynamics play in the ionosphere–thermosphere system.
3. Under low levels of local magnetic activity ($|\Delta H| \lesssim 40$ nT), the effect of the neutral dynamo was to increase the Joule heating rate, and the magnitude of the increase on average peaked approximately 1 h before magnetic midnight during the campaign. For $|\Delta H| \geq 40$ nT, the effect was to reduce the Joule heating rate, in agreement with the results of Cierpka et al. (2000), and in qualitative agreement with the simulation results of Thayer (1992).
4. Use of the ambipolar diffusion equation for calculation of the ion–neutral collision frequency requires very quiet geomagnetic conditions, conditions which are often difficult to obtain at high latitudes. By extrapolating the measured terms in the diffusion equation back to a 'zero activity' level, we were able to obtain a single estimate of the ion–neutral collision frequency (corresponding to an altitude of 260 km) from 8 days of campaign data

$$\nu_{in} = 1.02^{+0.179}_{-0.152}\ \mathrm{s}^{-1} \quad (26)$$

5. Extrapolating the neutral composition back to the 'zero activity' level gave the fractional number density of O as 75% (at 260 km), and this was used to estimate the O^+-O collision frequency as

$$\nu_{(O^+,O)} = 0.766^{+0.134}_{-0.114}\ \mathrm{s}^{-1} \quad (27)$$

This estimate lies between the values calculated from expressions given by Schunk and Walker (1973) and Hickman et al. (1997), both of which are within the 1σ experimental uncertainty of the current result.

The SDI has the ability to map neutral winds and temperatures at multiple altitudes by using different wavelength filters. PFISR is able to sample along multiple range-resolved beams essentially simultaneously, providing volumetric measurements of the ionosphere. Both instruments can be configured to operate routinely in these modes. As such, routine observations of ion–neutral coupling through direct (spatially resolved) measurement of both plasma and neutral dynamics are now possible, and such coordinated observations in conjunction with ground-based all-sky cameras and magnetometers could provide a unique and extensive database for future studies of high-latitude ion–neutral interactions, particularly as we move toward the peak of the current solar cycle.

Acknowledgements

Data collection and analysis for PFISR was supported under NSF cooperative agreements ATM-0608577 and AGS-1133009 to SRI International. Measurements of Hemispheric Power from the NOAA POES satellite are made available by the National Weather Service through the Space Weather Prediction Center (www.swpc.noaa.gov).

References

Aruliah, A.L., Rees, D., 1995. The trouble with thermospheric vertical winds: geomagnetic, seasonal and solar cycle dependence at high latitudes. Journal of Atmospheric and Terrestrial Physics 57 (6), 597–609.

Aruliah, A.L., Griffin, E.M., McWhirter, I., Aylward, A.D., Ford, E.A.K., Charalambous, A., Kosch, M.J., Davis, C.J., Howells, V.S.C., 2004. First tristatic studies of mesoscale ion–neutral dynamics and energetics in the high-latitude upper atmosphere using collocated FPIs and EISCAT radar. Geophysical Research Letters 31, L03,802, http://dx.doi.org/10.1029/2003GL018469.

Aruliah, A.L., et al., 2005. First direct evidence of meso-scale variability on ion–neutral dynamics using co-located tristatic FPIs and EISCAT radar in Northern Scandinavia. Annals of Geophysics 23, 147–162.

Banks, P.M., Kockarts, G., 1973. Aeronomy: Part B. Academic Press.

Brekke, A., Rino, C.L., 1978. High-resolution altitude profiles of the auroral zone energy dissipation due to ionospheric currents. Journal of Geophysical Research 83 (A6), 2517–2524.

Burchill, J.H., Clemmons, J.H., Knudsen, D.J., Larsen, M., Nicolls, M.J., Pfaff, R.F., Rowland, D., Sangalli, L., 2012. High-latitude E region ionosphere-thermosphere coupling: A comparative study using in situ and incoherent scatter radar observations. Journal of Geophyscial Research 117, http://dx.doi.org/10.1029/2011JA017175.

Burnside, R.G., Behnke, R.A., Walker, J.C.G., 1983. Meridional neutral winds in the thermosphere at Arecibo: simultaneous incoherent scatter and airglow observations. Journal of Geophysical Research 88 (A4), 3181–3189.

Burnside, R.G., Tepley, C.A., Wickwar, V.B., 1987. The O^+–O collision cross-section: can it be inferred from aeronomical measurements. Annals of Geophysics 5A (6), 343–350.

Cierpka, K., Kosch, M.J., Rietveld, M., Schlegel, K., Hagfors, T., 2000. Ion–neutral coupling in the high-latitude F-layer from incoherent scatter and Fabry–Perot interferometer measurements. Annals of Geophysics 18, 1145–1153.

Cole, K.D., 1962. Joule heating of the upper atmosphere. Australian Journal of Physics 15, 223–235.

Conde, M., Smith, R.W., 1995. Mapping thermospheric winds in the auroral zone. Geophysical Research Letters 22 (22), 3019–3022.

Conde, M., Smith, R.W., 1997. Phase compensation' of a separation scanned, all-sky imaging Fabry-Perot spectrometer for auroral studies. Applied Optics 36, 5441–5450.

Conde, M., Smith, R.W., 1998. Spatial structure in the thermospheric horizontal wind above Poker Flat, Alaska, during solar minimum. Journal of Geophysical Research 103 (A5), 9449–9472.

Dalgarno, A., 1964. Ambipolar diffusion in the F-region. Journal of Atmospheric and Terrestrial Physics 26, 939.

Davis, C.J., Farmer, A.D., Aruliah, A., 1995. An optimised method for calculating the O^+–O collision parameter from aeronomical measurements. Annals of Geophysics 13, 541–550, http://dx.doi.org/10.1007/s00585-995-0541-x.

de Meneses, F.C., Muralikrishna, P., Clemesha, B.R., 2008. Height profiles of OI 630 nm and OI 557.7 nm airglow intensities measured via rocket-borne photometers and estimated using electron density data: a comparison. Geofisica Internationale 47 (3), 161–166.

Deng, W., Killeen, T.L., Burns, A.G., Roble, R.G., Slavin, J.A., Wharton, L.E., 1993. The effects of neutral inertia on ionospheric currents in the high-latitude thermosphere following a geomagnetic storm. Journal of Geophysical Research 98 (A5), 7775–7790.

Fla, T., Kirkwood, S., Schlegel, K., 1985. Collision frequency measurements in the high-latitude *E* region with EISCAT. Radio Science 20 (4), 785–793.

Griffin, E.M., Aruliah, A.L., McWhirter, I., Yiu, H.-C.I., Charalambous, A., McCrea, I., 2008. Upper thermospheric neutral wind and temperature measurements from an extended spatial field. Annals of Geophysics 26, 2649–2655.

Gustafsson, G., Papitashvili, N.E., Papitashvili, V.O., 1992. A revised corrected geomagnetic coordinate system for epochs 1985 and 1990. Journal of Atmospheric and Terrestrial Physics 54, 1609–1631.

Heppner, J.P., Liebrecht, M.C., Maynard, N.C., Pfaff, R.F., 1993. High-latitude distributions of plasma waves and spatial irregularities from DE 2 alternating current electric field observations. Journal of Geophysical Research 98 (A2), 1629–1652.

Hickman, A.P., Medikeri-Naphade, M., Chapin, C.D., Huestis, D.L., 1997. Fine structure effects in the O^+–O collision frequency. Geophysical Research Letters 24 (2), 119–122.

Holmes, J.M., Conde, M., Deehr, C., Lummerzheim, D., 2005. Morphology of evening sector aurorae in λ557.7−nm Doppler temperatures. Geophysical Research Letters 32 (2), L02103, http://dx.doi.org/10.1029/2004GL021553.

Huuskonen, A., Nygén, T., Jalonen, L., Turunen, T., Silén, J., 1986. High resolution EISCAT observations of the ion–neutral collision frequency in the lower E-region. Journal of Atmospheric and Terrestrial Physics 48 (9–10), 827–836.

Killeen, T.L., Hays, P.B., Carignan, G.R., Heelis, R.A., Hanson, W.B., Spencer, N.W., Brace, L.H., 1984. Ion–neutral coupling in the high-latitude *F* region: evaluation of ion heating terms from Dynamics Explorer 2. Journal of Geophysical Research 89 (A9), 7495–7508.

Kirkwood, S., 1986. Seasonal and tidal variations of neutral temperatures and densities in the high latitude lower thermosphere measured by EISCAT. Journal of Atmospheric and Terrestrial Physics 48 (9–10), 817–826.

Kosch, M.J., Cierpka, K., Rietveld, M.T., Hagfors, T., Schlegel, K., 2001. High-latitude ground-based observations of the thermospheric ion–drag time constant. Geophysical Research Letters 28, 1395–1398.

Kosch, M.J., et al., 2011. Mesoscale observations of Joule heating near an auroral arc and ion–neutral collision frequency in the polar cap *E* region. Journal of Geophysical Research 116, A05,321, http://dx.doi.org/10.1029/2010JA016015.

Lathuillére, C., Wickwar, V.B., Kofman, W., 1983. Incoherent scatter measurements of ion–neutral collision frequencies and temperatures in the lower thermosphere of the auroral region. Journal of Geophysical Research 88 (A12), 10,137–10,144.

Lyons, L.R., Killeen, T.L., Walterscheid, R.L., 1985. The neutral wind 'flywheel' as a source of quiet-time polar-cap currents. Geophysical Research Letters 12 (2), 101–104.

Moffett, R.J., Sellek, R., Bailey, G.J., 1990. The influence of O^+–O collision frequency on ionospheric F-region behaviour. Journal of Atmospheric and Terrestrial Physics 52 (2), 125–132.

Nagy, A.F., Cicerone, R.J., Hays, P.B., McWatters, K.D., Meriwether, J.W., Belon, A.E., Rino, C.L., 1974. Simultaneous measurement of ion and neutral motions by radar and optical techniques. Radio Science 9 (2), 315–321.

Nicolls, M.J., Heinselman, C.J., 2007. Three-dimensional measurements of traveling ionospheric disturbances with the Poker Flat Incoherent Scatter Radar. Geophysical Research Letters 34, L2 1104, http://dx.doi.org/10.1029/2007GL03150.

Nygrén, T., 1996. Studies of the E-Region ion–neutral collision frequency using the EISCAT incoherent scatter radar. 18(3), 79–82.

Omidvar, K., Menard, R., Buonsanto, M.J., 1998. Empirical determination of the O^+–O collision frequency. Journal of Atmospheric and Solar-Terrestrial Physics 60, 1485–1496.

Pesnell, W.D., Omidvar, K., Hoegy, W.R., 1993. Momentum transfer collision frequency of O^+–O. Geophysical Research Letters 20, 1343–1346.

Reddy, C.A., Hoegy, W.R., Pesnell, W.D., Mayr, H.G., Hines, C.O., 1994. Accuracy of O^+–O collision cross section deduced from ionosphere–thermosphere observations. Geophysical Research Letters 21, 2429–2432.

Rees, D., Lloyd, N., Charleton, P.J., Carlson, M., Murdin, J., Häggström, I., 1984. Comparison of plasma flow and thermospheric circulation over northern Scandinavia using EISCAT and a Fabry–Perot interferometer. Journal of Atmospheric and Terrestrial Physics 46 (6/7), 545–564.

Richards, P.G., Nicolls, M.J., Heinselman, C.J., Sojka, J.J., Holt, J.M., Meier, R.R., 2009. Measured and modeled ionospheric densities, temperatures, and winds during the international polar year. Journal of Geophysical Research 114, A12,317, http://dx.doi.org/10.1029/2009JA014625.

Richards, P.G., Bilitza, D., Voglozin, D., 2010. Ion density calculator (IDC): a new efficient model of ionospheric ion densities. Radio Science 45, RS5007, http://dx.doi.org/10.1029/2009RS004332.

Roble, R.G., Rees, M.H., 1977. Time-dependent studies of the aurora: effects of particle precipitation on the dynamic morphology of ionospheric an atmospheric properties. Planetary and Space Science 25, 991–1010.

Salah, J.E., 1993. Interim standard for the ion–neutral atomic oxygen collision frequency. Geophysical Research Letters 20 (15), 1543–1546.

Sangalli, L., Knudsen, D.J., Larsen, M.F., Zhan, T., Pfaff, R.F., Rowland, D., 2009. Rocket-based measurements of ion velocity, neutral wind, and electric field in the collisional transition region of the auroral ionosphere. Journal of Geophysical Research 114, A04,306, http://dx.doi.org/10.1029/2008JA013757.

Schlegel, K., Kohl, H., Rinnert, K., 1980. Temperatures and collision frequency in the polar *E* region measured with the incoherent scatter technique. Journal of Geophysical Research 85 (A2), 710–714.

Schunk, R.W., Nagy, A.F., 2009. Ionospheres: Physics, Plasma Physics, and Chemistry, Cambridge Atmospheric and Space Science Series, 2nd ed. Cambridge University Press.

Schunk, R.W., Walker, J.C.G., 1973. Theoretical ion densities in the lower ionosphere. Planetary and Space Science 21, 1875–1896.

Semeter, J., Butler, T.W., Zettergren, M., Heinselman, C.J., Nicolls, M.J., 2010. Composite imaging of auroral forms and convective flows during a substorm cycle. Journal of Geophysical Research 115, A08,308, http://dx.doi.org/10.1029/2009JA014931.

Sobral, J.H.A., Takahashi, H., Abdu, M.A., Muralikrishna, P., Sahai, Y., Zamlutti, C.J., de Paula, E.R., Batista, P.P., 1993. Determination of the quenching rate of the $O(^1D)$ by $O(^3P)$ from rocket-borne optical (630 nm) and electron density data. Journal of Geophysical Research 98 (A5), 7791–7798.

St.-Maurice, J.-P., Cussenot, C., Kofman, W., 1999. On the usefulness of E region electron temperatures and lower F region ion temperatures for the extraction of thermospheric parameters: a case study. Annals of Geophysics 17, 1182–1198.

Stallcop, J.R., Partridge, H., Levin, E., 1991. Resonant charge transfer, transport cross section, and collision integrals for $N^+(^3P)$–$N(^4S^0)$ and $O^+(^4S^0)$–$O(^3P)$ interactions. Journal of Chemical Physics 95, 6429–6439.

Stubbe, P., 1968. Frictional forces and collision frequencies between moving ion and neutral gases. Journal of Atmospheric and Terrestrial Physics 30, 1965–1985.

Thayer, J.P., 1992. On the contribution of the thermospheric neutral wind to high-latitude energetics. Geophysical Research Letters 19 (3), 265–268.

Thayer, J.P., Crowley, G., Niciejewski, R.J., Killeen, T.L., Buchau, J., Reinisch, B.W., 1995a. Ground-based observations of ion/neutral coupling at Thule and Qânâq, Greenland. Journal of Geophysical Research 100 (A7), 12,189–12,199.

Thayer, J.P., Vickrey, J.F., Heelis, R.A., Gary, J.B., 1995b. Interpretation and modeling of the high-latitude electromagnetic energy flux. Journal of Geophysical Research 100 (A10), 19,715–19,728.

Wu, Q., Wang, W., Roble, R.G., Häggström, Ingemar, Strømme, Anja, 2012. First daytime thermospheric wind observation from a balloon-borne Fabry–Perot interferometer over Kiruna (68N). Geophysical Research Letters 39, L14104, http://dx.doi.org/10.1029/2012GL052533.

Wickwar, V.B., Meriwether, J.W., Hays, P.B., Nagy, A.F., 1984. The meridional thermospheric neutral wind measured by radar and optical techniques in the auroral region. Journal of Geophysical Research 89 (A12), 10,987–10,998.

Winser, K.J., Farmer, A.D., Rees, D., Aruliah, A., 1988. Ion–neutral dynamics in the high latitude ionosphere: first results from the INDI experiment. Journal of Atmospheric and Terrestrial Physics 50 (4–5), 369–377.